JOURNAL OF SPACECRAFT AND ROCKETS
Vol. 38, No. 4, July–August 2001

Numerical Simulation of Three-Dimensional Augmented Burnett Equations for Hypersonic Flow

Keon-Young Yun* and Ramesh K. Agarwal†
Wichita State University, Wichita, Kansas 67260-0093

For computation of hypersonic flowfields about space vehicles in low Earth orbits, where the local Knudsen numbers *Kn* lie in the continuum-transition regime, a set of extended three-dimensional hydrodynamic equations is required that is more accurate than the Navier–Stokes equations and computationally more efficient than the direct simulation Monte Carlo (DSMC) computations. The three-dimensional augmented Burnett equations are derived from the Chapman–Enskog expansion of the Boltzmann equation to $\mathcal{O}(Kn^2)$ and adding the augmented terms (linear third-order super Burnett terms with coefficients determined from linearized stability analysis to ensure stability of the augmented Burnett equations to small wavelength disturbances). The three-dimensional augmented Burnett equations are applied to compute the hypersonic blunt-body flows for various range of Knudsen numbers ($0.0884 \le Kn \le 0.227$) and Mach numbers ($10 \le M \le 25.3$). The computational results are compared with the Navier–Stokes solutions, the existing augmented Burnett solutions, and the available DSMC results. The comparisons show that the difference between the Navier–Stokes and the augmented Burnett solutions is very small (less than 3% for the shock layer thickness) at Knudsen numbers less than 0.01; the difference becomes significant as the Knudsen number increases. The comparisons also show that the augmented Burnett solutions are significantly closer to the DSMC results for the temperature distributions in the continuum-transition regime than the Navier–Stokes calculations.

Nomenclature

$\boldsymbol{E}$ = total flux vector in x direction
$\boldsymbol{E}_I$ = convective flux vector in x direction
$\boldsymbol{E}_V$ = viscous flux vector in x direction
e_t = total energy per unit mass
$\boldsymbol{F}$ = total flux vector in y direction
$\boldsymbol{F}_I$ = convective flux vector in y direction
$\boldsymbol{F}_V$ = viscous flux vector in y direction
$\boldsymbol{G}$ = total flux vector in z direction
$\boldsymbol{G}_I$ = convective flux vector in z direction
$\boldsymbol{G}_V$ = viscous flux vector in z direction
Kn = Knudsen number
L = reference length
M = Mach number
P = pressure
Pr = Prandtl number
$\boldsymbol{Q}$ = unknown vector in physical domain
$\boldsymbol{q}_i$ = heat flux terms
R = gas constant
Re = Reynolds number
r_n = nose radius
T = temperature
T_w = wall temperature
u = velocity components in x direction
v = velocity components in y direction
w = velocity components in z direction
$\bar{\alpha}$ = accommodation coefficient for wall surface
α_i, β_i = coefficients of stress terms in augmented Burnett equations
γ = specific heat ratio
γ_i = coefficients of heat flux terms in augmented Burnett equations
θ_i = coefficients of heat flux terms in augmented Burnett equations
κ = thermal conductivity
λ = mean free path of gas molecules
μ = viscosity
ρ = density
σ_{ij} = stress tensor
$\bar{\sigma}$ = reflection coefficient for wall surface
ω_i = coefficients of stress terms in augmented Burnett equations
ϖ = circular frequency of perturbation

Introduction

VARIOUS portions in the flight envelope of space vehicles may be broadly classified into the continuum, continuum-transition, and free molecular regimes. The Boltzmann equation describes the flows in all of the regimes.[1,2] However, it is very difficult to obtain closed-form analytic solutions except for the simplest of flows that are largely of academic interest. For practical problems, approximation techniques need to be applied to the Boltzmann equation to obtain meaningful solutions. The techniques available for solving the Boltzmann equation can be classified into the particle methods and the moment methods. The direct simulation Monte Carlo (DSMC) falls in the category of particle methods.[3,4] Moment methods derive the higher-order fluid dynamics approximations beyond Navier–Stokes equations to account for departures from thermal equilibrium. The higher-order fluid dynamic models are known as the extended hydrodynamic equations or the generalized hydrodynamic equations. However, both classes of methods have significant limitations, either in describing the physics or in terms of the computational resources needed for accurate simulations, for modeling flows in continuum-transition regime where the mean free path of the molecules is of the same order of magnitude as the characteristic length ($Kn \sim 1$).

In the continuum-transition regime, because there are hardly any ground-test facilities to provide wind-tunnel data and the flight data are very difficult to obtain, the only alternative is a numerical simulation. Currently, the DSMC method perhaps can be considered as the most accurate and widely used technique for computations of low-density flows. However, in the continuum-transition regime, where the densities are not low enough, the DSMC method requires a large number of particles for accurate simulations, which makes this

---

Received 11 February 2000; revision received 2 May 2000; accepted for publication 14 March 2001. Copyright © 2001 by Keon-Young Yun and Ramesh K. Agarwal. Published by the American Institute of Aeronautics and Astronautics, Inc., with permission.

*Research Associate, Department of Aerospace Engineering, National Institute for Aviation Research.

†Bloomfield Distinguished Professor and Executive Director, Department of Aerospace Engineering, National Institute for Aviation Research. Fellow AIAA

technique prohibitively expensive both in terms of computational time and memory requirements. As a result, higher-order extended hydrodynamic equations based on the continuum approach have been proposed that can model both the continuum and continuum-transition regimes and are computationally efficient.

In the continuum-transition regime, the linear stress–strain, linear heat flux, and temperature gradient relations break down as the Knudsen number increases. Consequently, there is a need for higher-order constitutive relations to model the stress and heat transfer terms properly. One of the methods in this approach exploits the Chapman–Enskog expansion[1] of the Boltzmann equation with Knudsen number as a parameter. In the Chapman–Enskog expansion, the first three terms in the expansion give a distribution function that results in nonlinear second-order constitutive relations in the Burnett equations, which represent a second-order departure from the thermal equilibrium. At low altitudes ($Kn < 0.01$), the gas flow does not depart significantly from the thermal equilibrium; therefore, the contribution of terms higher than the first-order terms in the constitutive relations is negligible. Thus, the Navier–Stokes equations are adequate to model the flow at low altitudes. However, as the altitude increases, the flow behavior increasingly departs from the equilibrium. Consequently, the second-order terms in the Burnett equations become important.

In 1988, Fiscko and Chapman[5,6] showed that the Burnett equations provide much more accurate numerical solutions than the Navier–Stokes equations for one-dimensional hypersonic shock structure in monatomic gases. However, Fiscko and Chapman found instability problems when the computational grids became finer than some critical value of the mean free path. This instability was predicted by Bobylev,[7] who showed that the linearized Burnett equations were unstable to perturbations of wavelength less than some critical value of the order of a mean free path.

In a subsequent attempt at solving the conventional Burnett equations in 1991, Zhong[8] showed that the Burnett equations could be stabilized by adding the linear third-order terms from the super Burnett equations. This set of equations was termed the augmented Burnett equations. The coefficients of these linear third-order terms were determined by carrying out a linearized stability analysis of the augmented Burnett equations. Zhong applied the augmented Burnett equations to compute the two-dimensional hypersonic flow over a blunt body and a space shuttle configuration in the continuum-transition regime. The augmented Burnett equations did not present any stability problems in computations of the hypersonic shock structure and hypersonic blunt-body flow. Furthermore, the calculations using the augmented Burnett equations agreed well with the DSMC results. Zhong and Furumoto,[9] in 1994, extended the two-dimensional augmented Burnett equations to three dimensions and obtained solutions for hypersonic flow past axisymmetric geometries. Again, the computations showed that the Burnett solutions were in closer agreement with the DSMC results than the Navier–Stokes solutions. However, Zhong[8] reported difficulties when the augmented Burnett equations were applied to compute the high Mach numbers ($M > 25$) blunt-body wake flows and flat plate boundary-layer flows. In computing these flows, it was observed that Burnett equations could orient the flow in a physically unrealistic manner by allowing shear layers to sharpen to discontinuities and permitting heat flow from cold to hot regions. Because this behavior is in violation of the second law of thermodynamics, it was conjectured that this entropy inconsistency may indeed be the cause of computational instability. Following this line of thought, a rigorous thermodynamic analysis of Burnett equations was performed by Comeaux et al.,[10] who showed that, when applied to hypersonic shock structure problem, Burnett equations can violate the second law of thermodynamics as the Knudsen number increases above a critical limit.

Recent computational investigations by Yun et al.[11] and Agarwal et al.[12] for blunt-body flows also show that the augmented Burnett equations are stable in the continuum-transition regime and that the solutions are in much closer agreement with the DSMC solutions than the Navier–Stokes solutions. Therefore, the Burnett equations are considered as an appropriate set of extended hydrodynamic equations for modeling this class of flows in continuum-transition regime. However, until now the augmented Burnett solutions have been obtained only for one-dimensional, two-dimensional, and axisymmetric flows. Thus, a three-dimensional augmented Burnett-equations-based code is needed for practical applications. The authors have extended the two-dimensional augmented Burnett equations to three dimensions.[13] The three-dimensional augmented Burnett equations and the results of its applications are presented in this paper.

Another important issue that has been a matter of considerable debate in the literature is as follows: What are the proper boundary conditions on the body surface for the Burnett equations, which contain second-order derivatives in the nonlinear shear stress and heat flux terms, in contrast to the Navier–Stokes equations, which have only first-order derivatives in the expressions for the linear shear stress and heat flux terms? In the continuum-transition regime, slip boundary conditions (velocity slip and temperature jump) are normally used on the body surface for the Navier–Stokes equations and the Burnett equations.[8,9] However, this issue remains unsolved at present. In this paper, slip boundary conditions are employed for both the Navier–Stokes equations and the Burnett equations.

Governing Equations

The governing equations for a three-dimensional unsteady compressible viscous flow can be written in Cartesian coordinates as

$$\frac{\partial \boldsymbol{Q}}{\partial t} + \frac{\partial \boldsymbol{E}}{\partial x} + \frac{\partial \boldsymbol{F}}{\partial y} + \frac{\partial \boldsymbol{G}}{\partial z} = 0 \tag{1}$$

where

$$\boldsymbol{Q} = \begin{bmatrix} \rho \\ \rho u \\ \rho v \\ \rho w \\ e_t \end{bmatrix} \tag{2}$$

The flux vectors, $\boldsymbol{E}$, $\boldsymbol{F}$, and $\boldsymbol{G}$ can be divided into the inviscid flux terms and the viscous flux terms as

$$\boldsymbol{E} = \boldsymbol{E}_I + \boldsymbol{E}_V \tag{3a}$$

$$\boldsymbol{F} = \boldsymbol{F}_I + \boldsymbol{F}_V \tag{3b}$$

$$\boldsymbol{G} = \boldsymbol{G}_I + \boldsymbol{G}_V \tag{3c}$$

where

$$\boldsymbol{E}_I = \begin{bmatrix} \rho u \\ \rho u^2 + p \\ \rho u v \\ \rho u w \\ (e_t + p) u \end{bmatrix}, \qquad \boldsymbol{E}_V = \begin{bmatrix} 0 \\ \sigma_{11} \\ \sigma_{12} \\ \sigma_{13} \\ \sigma_{11} u + \sigma_{12} v + \sigma_{13} w + q_1 \end{bmatrix} \tag{4a}$$

$$\boldsymbol{F}_I = \begin{bmatrix} \rho v \\ \rho u v \\ \rho v^2 + p \\ \rho v w \\ (e_t + p) v \end{bmatrix}, \qquad \boldsymbol{F}_V = \begin{bmatrix} 0 \\ \sigma_{21} \\ \sigma_{22} \\ \sigma_{23} \\ \sigma_{21} u + \sigma_{22} v + \sigma_{23} w + q_2 \end{bmatrix} \tag{4b}$$

$$\boldsymbol{G}_I = \begin{bmatrix} \rho w \\ \rho u w \\ \rho v w \\ \rho w^2 + p \\ (e_t + p) w \end{bmatrix}, \qquad \boldsymbol{G}_V = \begin{bmatrix} 0 \\ \sigma_{31} \\ \sigma_{32} \\ \sigma_{33} \\ \sigma_{31} u + \sigma_{32} v + \sigma_{33} w + q_3 \end{bmatrix} \tag{4c}$$

The constitutive equations for a gas flow near thermodynamic equilibrium can be derived as approximate solutions of the

Boltzmann equation using the Chapman–Enskog expansion. This method yields the general constitutive relations for the stress tensor σ_{ij} and heat flux vector $\boldsymbol{q}_i$ as follows:

$$\sigma_{ij} = \sigma_{ij}^{(0)} + \sigma_{ij}^{(1)} + \sigma_{ij}^{(2)} + \sigma_{ij}^{(3)} + \cdots + \sigma_{ij}^{(n)} + \mathcal{O}(Kn^{n+1}) \tag{5}$$

$$\boldsymbol{q}_i = \boldsymbol{q}_i^{(0)} + \boldsymbol{q}_i^{(1)} + \boldsymbol{q}_i^{(2)} + \boldsymbol{q}_i^{(3)} + \cdots + \boldsymbol{q}_i^{(n)} + \mathcal{O}(Kn^{n+1}) \tag{6}$$

where n is the order of accuracy with respect to Knudsen number Kn. The Knudsen number Kn is defined as

$$Kn = \lambda / L \tag{7}$$

where the mean free path λ is given by

$$\lambda = \frac{16\mu}{5\rho\sqrt{2\pi RT}} \tag{8}$$

In the case of $Kn \approx 0$, only the first term in Eqs. (5) and (6) is important. The zeroth-order approximation ($n = 0$) results in the Euler equations

$$\sigma_{ij}^{(0)} = 0 \tag{9a}$$

$$\boldsymbol{q}_i^{(0)} = 0 \tag{9b}$$

When $Kn < 0.1$, the first two terms in Eqs. (5) and (6) become important for accurate representation of stress and heat transfer properties of the gas flow. This first-order approximation represents the Navier–Stokes equations. The stress tensor and the heat flux terms ($n = 1$) in the three-dimensional Navier–Stokes equations are given as

$$\sigma_{11}^{(1)} = -\mu\left(\tfrac{4}{3}u_x - \tfrac{2}{3}v_y - \tfrac{2}{3}w_z\right) \tag{10a}$$

$$\sigma_{22}^{(1)} = -\mu\left(\tfrac{4}{3}v_y - \tfrac{2}{3}w_z - \tfrac{2}{3}u_x\right) \tag{10b}$$

$$\sigma_{33}^{(1)} = -\mu\left(\tfrac{4}{3}w_z - \tfrac{2}{3}u_x - \tfrac{2}{3}v_y\right) \tag{10c}$$

$$\sigma_{12}^{(1)} = \sigma_{21}^{(1)} = -\mu(u_y + v_x) \tag{10d}$$

$$\sigma_{23}^{(1)} = \sigma_{32}^{(1)} = -\mu(v_z + w_y) \tag{10e}$$

$$\sigma_{31}^{(1)} = \sigma_{13}^{(1)} = -\mu(w_x + u_z) \tag{10f}$$

$$q_1^{(1)} = -\kappa T_x \tag{10g}$$

$$q_2^{(1)} = -\kappa T_y \tag{10h}$$

$$q_3^{(1)} = -\kappa T_z \tag{10i}$$

As Knudsen number Kn becomes larger ($Kn > 0.1$), additional higher-order terms in Eqs. (5) and (6) are required. The second-order approximation yields the Burnett equations, which retain the first three terms in Eqs. (5) and (6). The three-dimensional expressions of the second-order stress and heat flux terms ($n = 2$) in the Burnett equations[13] are obtained as

$$\begin{aligned}
\sigma_{11}^{(2)} = \frac{\mu^2}{p}\bigg(&\alpha_1 u_x^2 + \alpha_2 u_y^2 + \alpha_3 u_z^2 + \alpha_4 v_x^2 + \alpha_5 v_y^2 + \alpha_6 v_z^2 + \alpha_7 w_x^2 \\
&+ \alpha_8 w_y^2 + \alpha_9 w_z^2 + \alpha_{10} u_x v_y + \alpha_{11} v_y w_z + \alpha_{12} w_z u_x + \alpha_{13} u_y v_x \\
&+ \alpha_{14} v_z w_y + \alpha_{15} w_x u_z + \alpha_{16} RT_{xx} + \alpha_{17} RT_{yy} + \alpha_{18} RT_{zz} \\
&+ \alpha_{19}\frac{RT}{\rho}\rho_{xx} + \alpha_{20}\frac{RT}{\rho}\rho_{yy} + \alpha_{21}\frac{RT}{\rho}\rho_{zz} + \alpha_{22}\frac{RT}{\rho^2}\rho_x^2 \\
&+ \alpha_{23}\frac{RT}{\rho^2}\rho_y^2 + \alpha_{24}\frac{RT}{\rho^2}\rho_z^2 + \alpha_{25}\frac{R}{T}T_x^2 + \alpha_{26}\frac{R}{T}T_y^2 + \alpha_{27}\frac{R}{T}T_z^2 \\
&+ \alpha_{28}\frac{R}{\rho}T_x\rho_x + \alpha_{29}\frac{R}{\rho}T_y\rho_y + \alpha_{30}\frac{R}{\rho}T_z\rho_z\bigg)
\end{aligned} \tag{11a}$$

$$\begin{aligned}
\sigma_{22}^{(2)} = \frac{\mu^2}{p}\bigg(&\alpha_1 v_y^2 + \alpha_2 v_z^2 + \alpha_3 v_x^2 + \alpha_4 w_y^2 + \alpha_5 w_z^2 + \alpha_6 w_x^2 + \alpha_7 u_y^2 \\
&+ \alpha_8 u_z^2 + \alpha_9 u_x^2 + \alpha_{10} v_y w_z + \alpha_{11} w_z u_x + \alpha_{12} u_x v_y + \alpha_{13} v_z w_y \\
&+ \alpha_{14} w_x u_z + \alpha_{15} u_y v_x + \alpha_{16} RT_{yy} + \alpha_{17} RT_{zz} + \alpha_{18} RT_{xx} \\
&+ \alpha_{19}\frac{RT}{\rho}\rho_{yy} + \alpha_{20}\frac{RT}{\rho}\rho_{zz} + \alpha_{21}\frac{RT}{\rho}\rho_{xx} + \alpha_{22}\frac{RT}{\rho^2}\rho_y^2 \\
&+ \alpha_{23}\frac{RT}{\rho^2}\rho_z^2 + \alpha_{24}\frac{RT}{\rho^2}\rho_x^2 + \alpha_{25}\frac{R}{T}T_y^2 + \alpha_{26}\frac{R}{T}T_z^2 + \alpha_{27}\frac{R}{T}T_x^2 \\
&+ \alpha_{28}\frac{R}{\rho}T_y\rho_y + \alpha_{29}\frac{R}{\rho}T_z\rho_z + \alpha_{30}\frac{R}{\rho}T_x\rho_x\bigg)
\end{aligned} \tag{11b}$$

$$\begin{aligned}
\sigma_{33}^{(2)} = \frac{\mu^2}{p}\bigg(&\alpha_1 w_z^2 + \alpha_2 w_x^2 + \alpha_3 w_y^2 + \alpha_4 u_z^2 + \alpha_5 u_x^2 + \alpha_{12} v_y w_z \\
&+ \alpha_{13} w_x u_z + \alpha_{14} u_y v_x + \alpha_{15} v_z w_y + \alpha_6 u_y^2 + \alpha_7 v_z^2 + \alpha_8 v_x^2 \\
&+ \alpha_9 v_y^2 + \alpha_{10} w_z u_x + \alpha_{11} u_x v_y + \alpha_{16} RT_{zz} + \alpha_{17} RT_{xx} \\
&+ \alpha_{18} RT_{yy} + \alpha_{19}\frac{RT}{\rho}\rho_{zz} + \alpha_{20}\frac{RT}{\rho}\rho_{xx} + \alpha_{21}\frac{RT}{\rho}\rho_{yy} \\
&+ \alpha_{22}\frac{RT}{\rho^2}\rho_z^2 + \alpha_{23}\frac{RT}{\rho^2}\rho_x^2 + \alpha_{24}\frac{RT}{\rho^2}\rho_y^2 + \alpha_{25}\frac{R}{T}T_z^2 + \alpha_{26}\frac{R}{T}T_x^2 \\
&+ \alpha_{27}\frac{R}{T}T_y^2 + \alpha_{28}\frac{R}{\rho}T_z\rho_z + \alpha_{29}\frac{R}{\rho}T_x\rho_x + \alpha_{30}\frac{R}{\rho}T_y\rho_y\bigg)
\end{aligned} \tag{11c}$$

$$\begin{aligned}
\sigma_{12}^{(2)} = \sigma_{21}^{(2)} = \frac{\mu^2}{p}\bigg(&\beta_1 u_x u_y + \beta_2 v_x v_y + \beta_3 w_x w_y + \beta_4 u_x v_x + \beta_5 u_y v_y \\
&+ \beta_6 u_z v_z + \beta_7 u_y w_z + \beta_8 v_x w_z + \beta_9 u_z w_y + \beta_{10} v_z w_x \\
&+ \beta_{11} RT_{xy} + \beta_{12}\frac{RT}{\rho}\rho_{xy} + \beta_{13}\frac{R}{T}T_x T_y + \beta_{14}\frac{RT}{\rho^2}\rho_x\rho_y \\
&+ \beta_{15}\frac{R}{\rho}\rho_x T_y + \beta_{16}\frac{R}{\rho}T_x\rho_y\bigg)
\end{aligned} \tag{11d}$$

$$\begin{aligned}
\sigma_{23}^{(2)} = \sigma_{32}^{(2)} = \frac{\mu^2}{p}\bigg(&\beta_1 v_y v_z + \beta_2 w_y w_z + \beta_3 u_y u_z + \beta_4 v_y w_y \\
&+ \beta_5 v_z w_z + \beta_6 v_x w_x + \beta_7 v_z u_x + \beta_8 w_y u_x + \beta_9 v_x u_z \\
&+ \beta_{10} w_x u_y + \beta_{11} RT_{yz} + \beta_{12}\frac{RT}{\rho}\rho_{yz} + \beta_{13}\frac{R}{T}T_y T_z \\
&+ \beta_{14}\frac{RT}{\rho^2}\rho_y\rho_z + \beta_{15}\frac{R}{\rho}\rho_y T_z + \beta_{16}\frac{R}{\rho}T_y\rho_z\bigg)
\end{aligned} \tag{11e}$$

$$\begin{aligned}
\sigma_{31}^{(2)} = \sigma_{13}^{(2)} = \frac{\mu^2}{p}\bigg(&\beta_1 w_z w_x + \beta_2 u_z u_x + \beta_3 v_z v_x + \beta_4 w_z u_z \\
&+ \beta_5 w_x u_x + \beta_6 w_y u_y + \beta_7 w_x v_y + \beta_8 u_z v_y + \beta_9 w_y v_x \\
&+ \beta_{10} u_y v_z + \beta_{11} RT_{zx} + \beta_{12}\frac{RT}{\rho}\rho_{zx} + \beta_{13}\frac{R}{T}T_z T_x \\
&+ \beta_{14}\frac{RT}{\rho^2}\rho_z\rho_x + \beta_{15}\frac{R}{\rho}\rho_z T_x + \beta_{16}\frac{R}{\rho}T_z\rho_x\bigg)
\end{aligned} \tag{11f}$$

$$q_1^{(2)} = \frac{\mu^2}{\rho}\left(\gamma_1\frac{1}{T}T_x u_x + \gamma_2\frac{1}{T}T_x v_y + \gamma_3\frac{1}{T}T_x w_z + \gamma_4\frac{1}{T}T_y v_x \right.$$

$$+ \gamma_5\frac{1}{T}T_y u_y + \gamma_6\frac{1}{T}T_z w_x + \gamma_7\frac{1}{T}T_z u_z + \gamma_8 u_{xx}$$

$$+ \gamma_9 u_{yy} + \gamma_{10} u_{zz} + \gamma_{11} v_{xy} + \gamma_{12} w_{xz} + \gamma_{13}\frac{1}{\rho}\rho_x u_x$$

$$+ \gamma_{14}\frac{1}{\rho}\rho_x v_y + \gamma_{15}\frac{1}{\rho}\rho_x w_z + \gamma_{16}\frac{1}{\rho}\rho_y v_x + \gamma_{17}\frac{1}{\rho}\rho_y u_y$$

$$\left. + \gamma_{18}\frac{1}{\rho}\rho_z w_x + \gamma_{19}\frac{1}{\rho}\rho_z u_z\right) \tag{11g}$$

$$q_2^{(2)} = \frac{\mu^2}{\rho}\left(\gamma_1\frac{1}{T}T_y v_y + \gamma_2\frac{1}{T}T_y w_z + \gamma_3\frac{1}{T}T_y u_x + \gamma_4\frac{1}{T}T_z w_y \right.$$

$$+ \gamma_5\frac{1}{T}T_z v_z + \gamma_6\frac{1}{T}T_x u_y + \gamma_7\frac{1}{T}T_x v_x + \gamma_8 v_{yy} + \gamma_9 v_{zz} + \gamma_{10} v_{xx}$$

$$+ \gamma_{11} w_{yz} + \gamma_{12} u_{xy} + \gamma_{13}\frac{1}{\rho}\rho_y v_y + \gamma_{14}\frac{1}{\rho}\rho_y w_z + \gamma_{15}\frac{1}{\rho}\rho_y u_x$$

$$\left. + \gamma_{16}\frac{1}{\rho}\rho_z w_y + \gamma_{17}\frac{1}{\rho}\rho_z v_z + \gamma_{18}\frac{1}{\rho}\rho_x u_y + \gamma_{19}\frac{1}{\rho}\rho_x v_x\right) \tag{11h}$$

$$q_3^{(2)} = \frac{\mu^2}{\rho}\left(\gamma_1\frac{1}{T}T_z w_z + \gamma_2\frac{1}{T}T_z u_x + \gamma_3\frac{1}{T}T_z v_y + \gamma_4\frac{1}{T}T_x u_z \right.$$

$$+ \gamma_5\frac{1}{T}T_x w_x + \gamma_6\frac{1}{T}T_y v_z + \gamma_7\frac{1}{T}T_y w_y + \gamma_8 w_{zz} + \gamma_9 w_{xx}$$

$$+ \gamma_{10} w_{yy} + \gamma_{11} u_{xz} + \gamma_{12} v_{yz} + \gamma_{13}\frac{1}{\rho}\rho_z w_z + \gamma_{14}\frac{1}{\rho}\rho_z u_x$$

$$+ \gamma_{15}\frac{1}{\rho}\rho_z v_y + \gamma_{16}\frac{1}{\rho}\rho_x u_z + \gamma_{17}\frac{1}{\rho}\rho_x w_x$$

$$\left. + \gamma_{18}\frac{1}{\rho}\rho_y v_z + \gamma_{19}\frac{1}{\rho}\rho_y w_y\right) \tag{11i}$$

The coefficients α_i, β_i, and γ_i in Eqs. (11a–11i) are given in the Appendix.

The expressions for the augmented stress and heat flux terms[13] are obtained as

$$\sigma_{11}^{(a)} = (\mu^3/p^2)RT[\alpha_{31}u_{xxx} + \alpha_{32}u_{xyy} + \alpha_{33}u_{xzz} + \alpha_{34}v_{xxy}$$

$$+ \alpha_{35}v_{yyy} + \alpha_{36}v_{yzz} + \alpha_{37}w_{xxz} + \alpha_{38}w_{yyz} + \alpha_{39}w_{zzz}] \tag{12a}$$

$$\sigma_{22}^{(a)} = (\mu^3/p^2)RT[\alpha_{31}v_{yyy} + \alpha_{32}v_{yzz} + \alpha_{33}v_{yxx} + \alpha_{34}w_{yyz}$$

$$+ \alpha_{35}w_{zzz} + \alpha_{36}w_{zxx} + \alpha_{37}u_{yyx} + \alpha_{38}u_{zzx} + \alpha_{39}u_{xxx}] \tag{12b}$$

$$\sigma_{33}^{(a)} = (\mu^3/p^2)RT[\alpha_{31}w_{zzz} + \alpha_{32}w_{zxx} + \alpha_{33}w_{zyy} + \alpha_{34}u_{zzx}$$

$$+ \alpha_{35}u_{xxx} + \alpha_{36}u_{xyy} + \alpha_{37}v_{zzy} + \alpha_{38}v_{xxy} + \alpha_{39}v_{yyy}] \tag{12c}$$

$$\sigma_{12}^{(a)} = \sigma_{21}^{(a)} = (\mu^3/p^2)RT[\beta_{17}u_{yxx} + \beta_{18}u_{yyy} + \beta_{19}u_{yzz}$$

$$+ \beta_{20}v_{xxx} + \beta_{21}v_{xyy} + \beta_{22}v_{xzz}] \tag{12d}$$

$$\sigma_{23}^{(a)} = \sigma_{32}^{(a)} = (\mu^3/p^2)RT[\beta_{17}v_{zxx} + \beta_{18}v_{zyy} + \beta_{19}v_{zzz}$$

$$+ \beta_{20}w_{yxx} + \beta_{21}w_{yyy} + \beta_{22}w_{yzz}] \tag{12e}$$

$$\sigma_{31}^{(a)} = \sigma_{13}^{(a)} = (\mu^3/p^2)RT[\beta_{17}w_{xxx} + \beta_{18}w_{xyy} + \beta_{19}w_{xzz}$$

$$+ \beta_{20}u_{zxx} + \beta_{21}u_{zyy} + \beta_{22}u_{zzz}] \tag{12f}$$

$$q_1^{(a)} = (\mu^3/p\rho)R[\gamma_{20}T_{xxx} + \gamma_{21}T_{xyy} + \gamma_{22}T_{xzz} + \gamma_{23}(T/\rho)\rho_{xxx}$$

$$+ \gamma_{24}(T/\rho)\rho_{xyy} + \gamma_{25}(T/\rho)\rho_{xzz}] \tag{12g}$$

$$q_2^{(a)} = (\mu^3/p\rho)R[\gamma_{20}T_{yxx} + \gamma_{21}T_{yyy} + \gamma_{22}T_{yzz} + \gamma_{23}(T/\rho)\rho_{yxx}$$

$$+ \gamma_{24}(T/\rho)\rho_{yyy} + \gamma_{25}(T/\rho)\rho_{yzz}] \tag{12h}$$

$$q_3^{(a)} = (\mu^3/p\rho)R[\gamma_{20}T_{zxx} + \gamma_{21}T_{zyy} + \gamma_{22}T_{zzz} + \gamma_{23}(T/\rho)\rho_{zxx}$$

$$+ \gamma_{24}(T/\rho)\rho_{zyy} + \gamma_{25}(T/\rho)\rho_{zzz}] \tag{12i}$$

The coefficients in Eqs. (12a–12i) are given as

$$\alpha_{31} = \alpha_{32} = \alpha_{33} = \omega_7$$

$$\alpha_{34} = \alpha_{35} = \alpha_{36} = \alpha_{37} = \alpha_{38} = \alpha_{39} = -\tfrac{1}{2}\omega_7$$

$$\beta_{17} = \beta_{18} = \beta_{19} = \beta_{20} = \beta_{21} = \beta_{22} = \tfrac{3}{4}\omega_7$$

$$\gamma_{20} = \gamma_{21} = \gamma_{22} = \theta_7, \qquad \gamma_{23} = \gamma_{24} = \gamma_{25} = \theta_6$$

To determine the coefficients ω_7, θ_6, and θ_7 of the augmented terms for stable solutions, the linearized stability analysis of the three-dimensional augmented Burnett equations is performed. This analysis is presented in the following section.

The stress and heat flux terms of the three-dimensional augmented Burnett equations are obtained by combining the first-, second-, and augmented-order expressions of stress and heat flux terms as

$$\sigma_{ij} = \sigma_{ij}^{(1)} + \sigma_{ij}^{(2)} + \sigma_{ij}^{(a)} \tag{13}$$

$$\boldsymbol{q}_i = \boldsymbol{q}_i^{(1)} + \boldsymbol{q}_i^{(2)} + \boldsymbol{q}_i^{(a)} \tag{14}$$

Finally, the governing Eqs. (1), (13), and (14) are nondimensionalized by a reference length and freestream variables and are written in a curvilinear coordinate system (ξ, η, ζ) by employing a coordinate transformation:

$$\xi = \xi(x, y, z), \qquad \eta = \eta(x, y, z), \qquad \zeta = \zeta(x, y, z) \tag{15}$$

Linearized Stability Analysis

The three-dimensional augmented Burnett equations were linearized by neglecting products and powers of small perturbations, and a linearized set of equations for small perturbation variables $\boldsymbol{V}' = [\rho', u', v', w', T']^T$ was obtained.[13] It was assumed that the solution is of the form

$$\boldsymbol{V}' = \bar{\boldsymbol{V}} \cdot e^{i\varpi x'} \cdot e^{i\varpi y'} \cdot e^{i\varpi z'} \cdot e^{\phi t'} \tag{16}$$

where $\phi = \alpha + i\beta$ and α and β denote the attenuation and dispersion coefficients, respectively. The circular frequency of the periodic perturbation ϖ is assumed to be the same in each direction to simplify the analysis. For stability, $\alpha \leq 0$ as the Knudsen number increases. Substitution of Eq. (16) into the equations for small perturbation quantities $\boldsymbol{V}'$ results in a characteristic equation $|F(\phi, \varpi)| = 0$. The trajectory of the roots of this characteristic equation is plotted in a complex plane on which the real axis denotes the attenuation coefficient and the imaginary axis denotes the dispersion coefficient.

Figure 1 shows the characteristic trajectories of the three-dimensional conventional Burnett equations for the Maxwellian gas. In Fig. 1, without the augmented terms, the trajectories of the conventional Burnett equations move into the unstable region ($\alpha > 0$). Therefore, the coefficients ω_7, θ_6, and θ_7 in the augmented terms must be chosen to stabilize the conventional Burnett equations. The coefficients from the super Burnett equations for Maxwellian gas are considered first. These coefficients are

$$\omega_7 = \tfrac{2}{9}, \qquad \theta_6 = -\tfrac{5}{8}, \qquad \theta_7 = -\tfrac{157}{16}$$

Figure 2 shows that the three-dimensional Burnett equations are not stable if the preceding coefficients are used. The condition for the three-dimensional augmented Burnett equations to be stable, with $\omega_7 = \frac{2}{9}$ and $\theta_6 = -\frac{5}{8}$, is $\theta_7 > \frac{5}{16}$. However, the coefficient θ_7

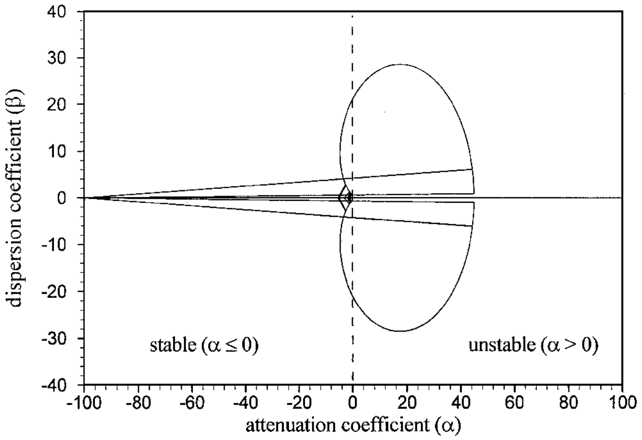

Fig. 1 Characteristic trajectories of the three-dimensional Burnett equations for a Maxwellian gas.

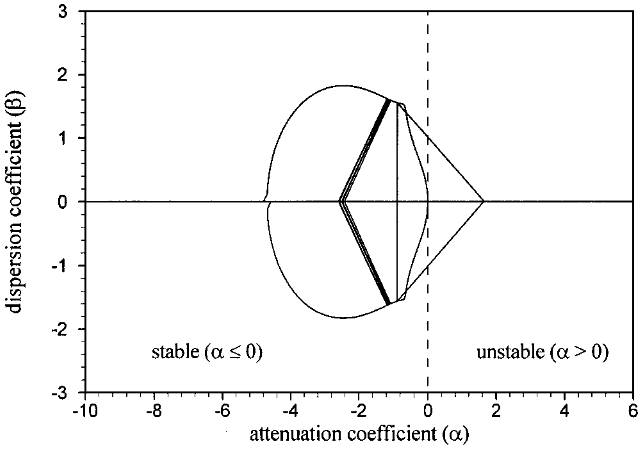

Fig. 2 Characteristic trajectories of the three-dimensional super Burnett equations for a Maxwellian gas.

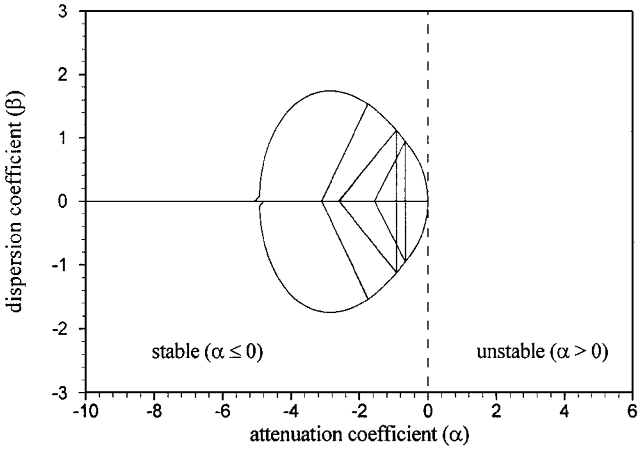

Fig. 3 Characteristic trajectories of the three-dimensional augmented Burnett equations for a Maxwellian gas.

is chosen to be $\frac{11}{16}$ to meet the preceding condition and to be the same as that proposed by Zhong[8] for the two-dimensional augmented Burnett equations. Figure 3 shows that characteristic trajectories of the three-dimensional augmented Burnett equations for a Maxwellian gas. The trajectories of the characteristic equation are always in the stable region. Therefore, the coefficients chosen satisfy the stability requirement for the three-dimensional augmented Burnett equations.

Boundary Conditions

Freestream conditions are used along the outer boundary. First-order extrapolation of the interior data is used to determine the flow properties along the exit boundary. The first-order Maxwell–Smoluchowski slip boundary conditions (see Ref. 14) are used on the wall surface boundary. The first-order Maxwell–Smoluchowski slip boundary conditions in Cartesian coordinates are

$$U_s = \frac{2-\bar{\sigma}}{\bar{\sigma}}\frac{2\mu}{\rho}\sqrt{\frac{\pi}{8RT}}\left(\frac{\partial U}{\partial y}\right)_s + \frac{3}{4}\frac{\mu}{\rho T}\left(\frac{\partial T}{\partial x}\right)_s \tag{17}$$

$$T_s = T_w + \frac{2-\bar{\alpha}}{\bar{\alpha}}\frac{2\gamma}{\gamma+1}\frac{2\mu}{\rho}\sqrt{\frac{\pi}{8RT}}\frac{1}{Pr}\left(\frac{\partial T}{\partial y}\right)_s \tag{18}$$

The subscript s denotes the flow variables on the solid surface of the body. The reflection coefficient $\bar{\sigma}$ and the accommodation coefficient $\bar{\alpha}$ are set to 1.

Numerical Method

An explicit finite difference scheme is employed to solve the governing equations. The Steger–Warming flux-vector splitting method[15] is applied to the inviscid flux terms. The second-order central differencing scheme is applied to discretize the stress tensor and heat flux terms.

Results and Discussion

The three-dimensional augmented Burnett equations are numerically solved for hypersonic flows past blunt bodies in the continuum-transition regime for gaseous mediums such as argon, hard-sphere gas, and air.

Case 1: Grid Convergence Studies

The three-dimensional grid convergence studies were performed on three sets of grids around a hemispherical nose with nose radius of 2.53 m. Three grids with 31 × 50 × 24 (grid A), 61 × 100 × 48 (grid B), and 91 × 150 × 48 (grid C) meshes were employed in a fixed physical domain. As an illustration, the side views of grids A and B are compared in Fig. 4. Computations were performed for the following flow conditions:

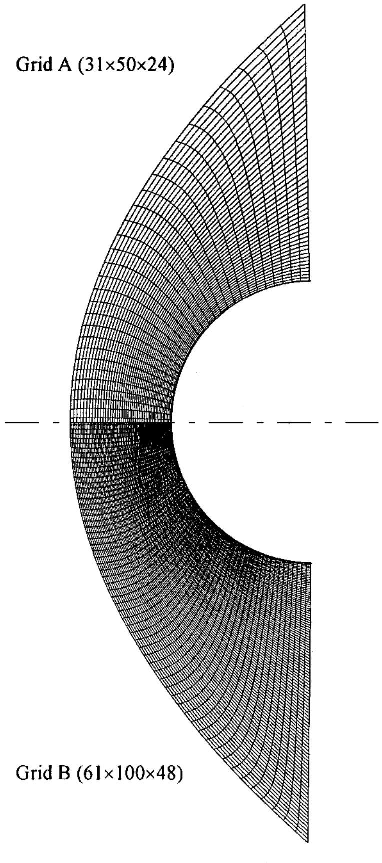

Fig. 4 Comparison of grids for case 1 (side views, r_n = 2.53 m).

$$M_\infty = 10.0, \qquad Kn_\infty = 0.0884, \qquad Re_\infty = 171$$

$$P_\infty = 0.02925\ \mathrm{N/m^2}, \qquad T_\infty = 230.8\ \mathrm{K}, \qquad T_w = 1111\ \mathrm{K}$$

The viscosity was calculated by the Sutherland's law. Other constants used in this computation for air are

$$\gamma = 1.4, \qquad Pr = 0.72, \qquad R = 287.04\ \mathrm{m^2/(s^2 \cdot K)}$$

The comparisons of density and temperature distributions along the stagnation streamline for the augmented Burnett solutions for grids A, B, and C are shown in Figs. 5 and 6, respectively. The results for grids B and C are the same for both density and temperature distributions. The results for grid A show a small difference with those of grids B and C in the temperature distribution in the shock layer. The augmented Burnett computations on grid C require much larger CPU time to obtain converged solution compared to grid B. Therefore, grid B is considered to be an adequate grid system for both maintaining the accuracy as well as the computational efficiency.

Case 2: Code Validation Test 1

For three-dimensional code validation, first the hypersonic flow of argon gas past a hemispherical nose with radius of 0.02 m at zero angle of attack is computed. The computational results are compared with those of Zhong and Furumoto[9] obtained with an axisymmetric augmented Burnett solver. The flow conditions for this test case are

$$M_\infty = 10.95, \qquad Kn_\infty = 0.2, \qquad Re_\infty = 90.3$$

$$P_\infty = 1.181\ \mathrm{N/m^2}, \qquad T_\infty = 300\ \mathrm{K}, \qquad T_w = 300\ \mathrm{K}$$

The argon gas is assumed to be a monatomic gas with hard-sphere model. The viscosity is calculated by the power law:

$$\mu = \mu_r (T/T_r)^{0.5} \tag{19}$$

The reference viscosity μ_r and the reference temperature T_r are taken as

$$\mu_r = 2.2695 \times 10^{-5}\ \mathrm{kg/s \cdot m}, \qquad T_r = 300\ \mathrm{K}$$

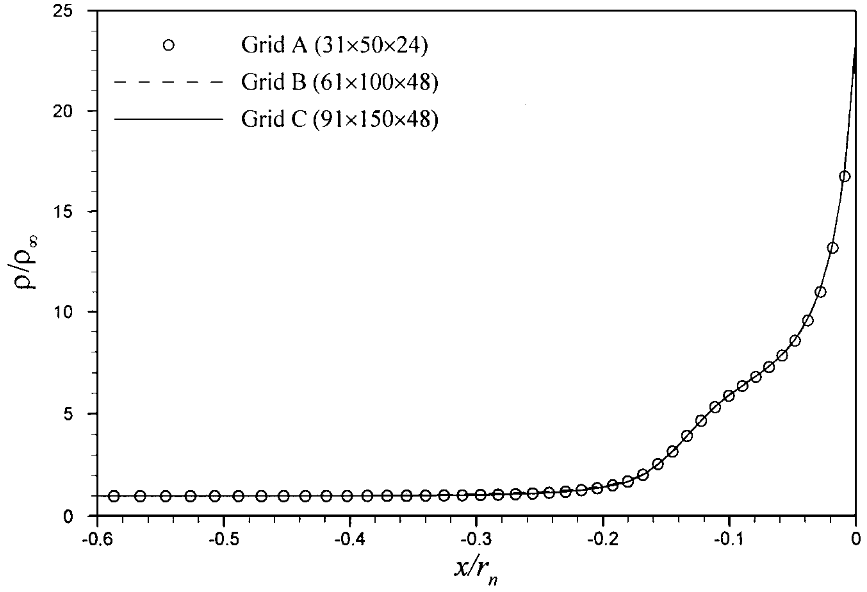

Fig. 5 Density distributions of augmented Burnett solutions along stagnation streamline for case 1: air, M_∞ = 10, and Kn_∞ = 0.0884.

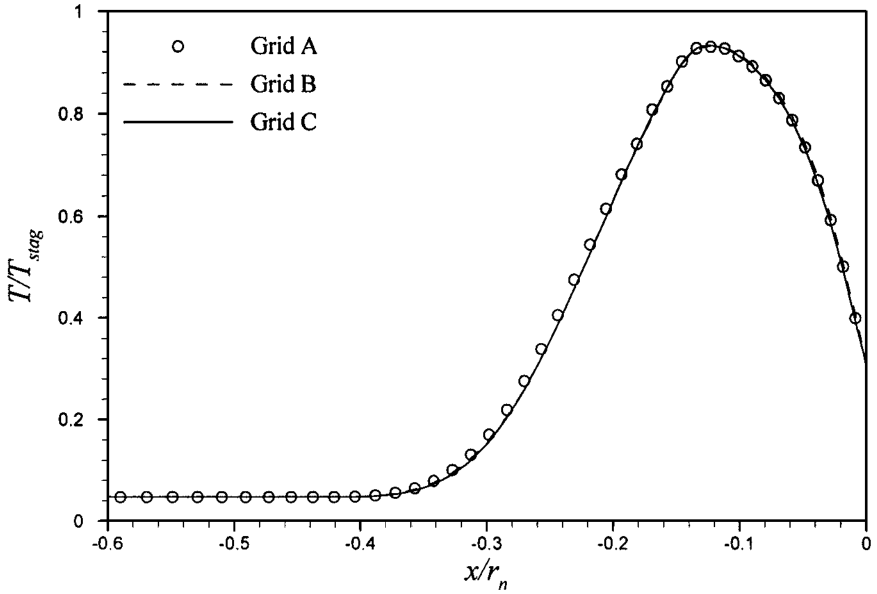

Fig. 6 Temperature distributions of augmented Burnett solutions along stagnation streamline for case 1: air, M_∞ = 10, and Kn_∞ = 0.0884.

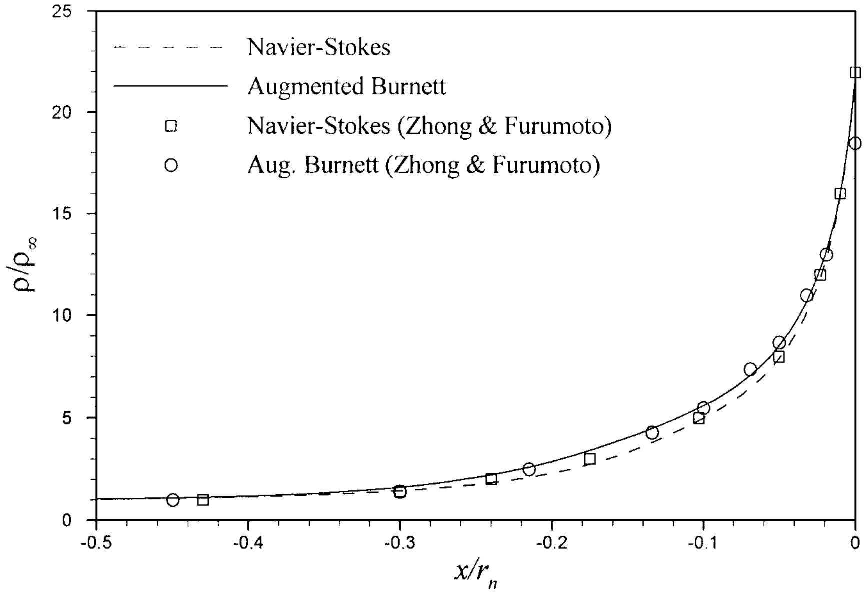

Fig. 7 Density distributions along stagnation streamline for case 2: argon, M_∞ = 10.95, and Kn_∞ = 0.2.

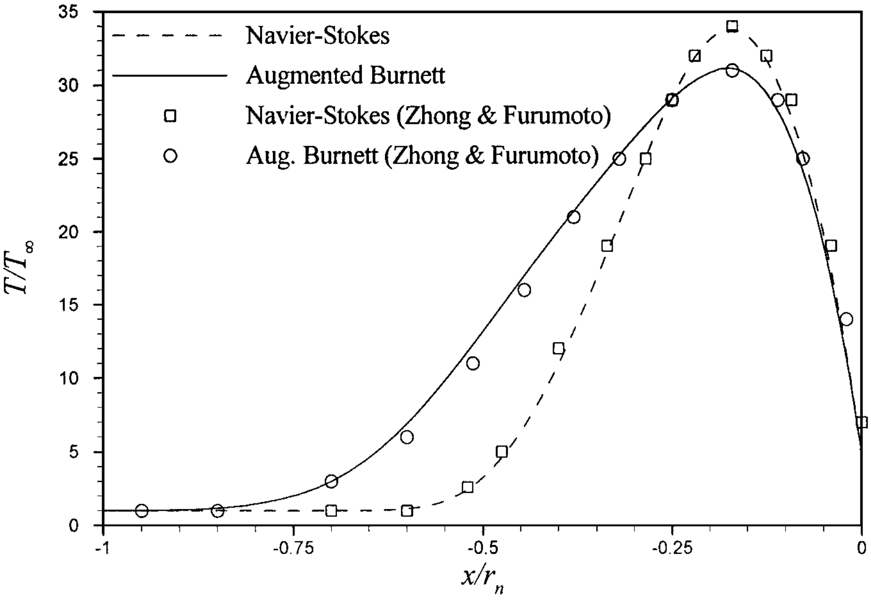

Fig. 8 Temperature distributions along stagnation streamline for case 2: argon, M_∞ = 10.95, and Kn_∞ = 0.2.

Other constants used in this computation are

$$\gamma = 1.67, \qquad Pr = 0.67, \qquad R = 208.13\ \mathrm{m^2/(s^2 \cdot K)}$$

The comparisons of density and temperature distributions along the stagnation streamline between the present three-dimensional augmented Burnett solver and the axisymmetric augmented Burnett solver of Zhong and Furumoto are shown in Figs. 7 and 8, respectively. The corresponding Navier–Stokes solutions are also compared in Figs. 7 and 8. The present three-dimensional augmented Burnett solutions agree well with those of Zhong's axisymmetric augmented Burnett solutions. The results show that the augmented Burnett equations predict about 35% thicker shock layer compared to the Navier–Stokes equations. The maximum temperature along the stagnation streamline predicted by the augmented Burnett equations is 9% lower than that predicted by the Navier–Stokes equations. However, the density distributions show a smaller difference between the two solutions.

Case 3: Code Validation Test 2

As a second test case in three-dimensional code validation, the results of the three-dimensional augmented Burnett computations are compared with the DSMC results obtained by Vogenitz and Takara[16] for the axisymmetric hemispherical nose. The computed results are also compared with Zhong and Furumoto's axisymmetric augmented Burnett solutions.[9] The flow conditions for this case are

$$M_\infty = 10, \qquad Kn_\infty = 0.1, \qquad T_w/T_\infty = 1.0, \qquad T_w/T_0 = 0.029$$

where T_0 is the stagnation temperature. The gas is assumed to be a monatomic gas with a hard-sphere model. The viscosity coefficient is calculated by the power law given by Eq. (19). The reference viscosity μ_r and the reference temperature T_r used in this test case are the same as for case 2.

The comparisons of density and temperature distributions along the stagnation streamline among the present three-dimensional augmented Burnett solutions, the axisymmetric augmented Burnett solutions of Zhong and Furumoto,[9] and the DSMC results are shown in Figs. 9 and 10, respectively. The corresponding Navier–Stokes solutions are also compared in Figs. 9 and 10. The present three-dimensional augmented Burnett solutions agree well with the Zhong and Furumoto axisymmetric augmented Burnett solutions in both density and temperature. The density distributions for both the Navier–Stokes and the augmented Burnett equations show

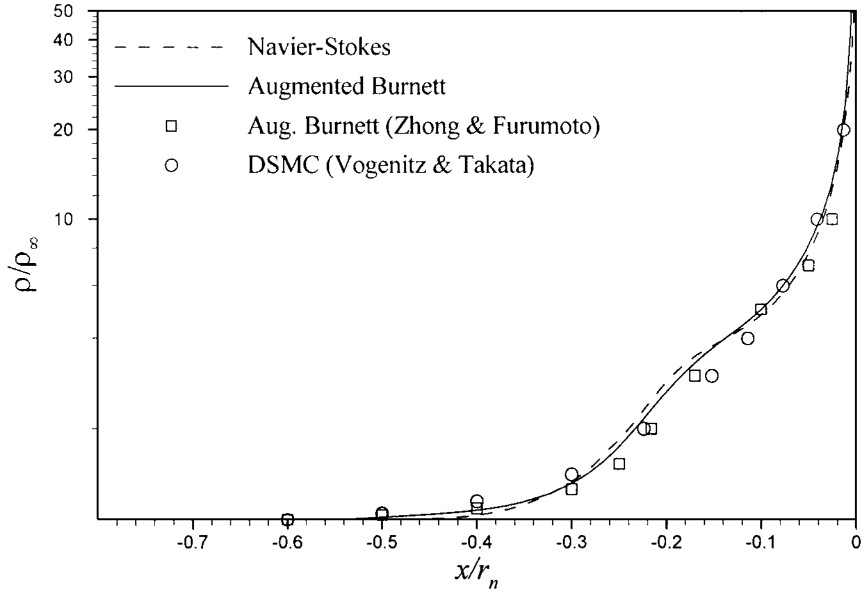

Fig. 9 Density distributions along stagnation streamline for case 3: hard-sphere gas, $M_\infty = 10$, and $Kn_\infty = 0.1$.

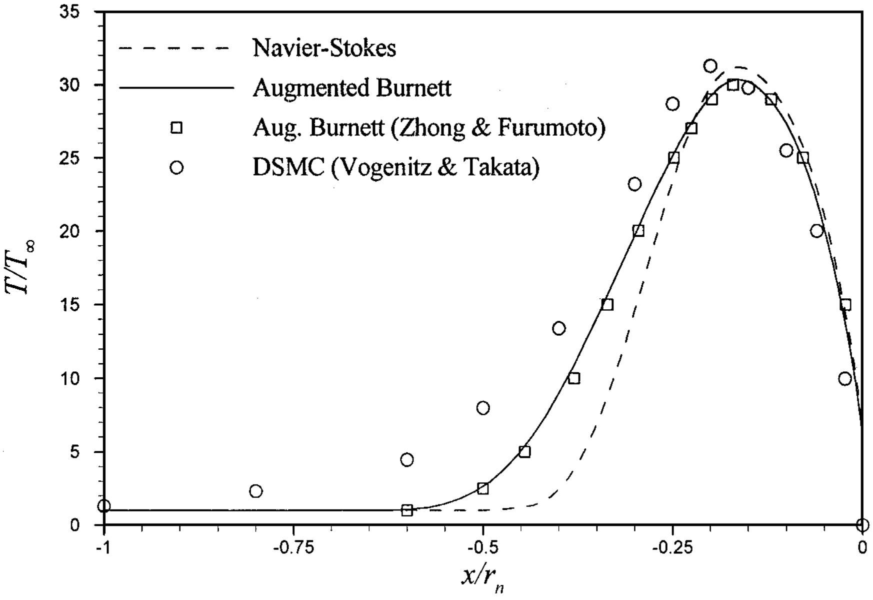

Fig. 10 Temperature distributions along stagnation streamline for case 3: hard-sphere gas, $M_\infty = 10$, and $Kn_\infty = 0.1$.

little difference from the DSMC results. The temperature distributions, however, show that the DSMC method predicts a thicker shock (~35%) than the augmented Burnett equations. The maximum temperature of the DSMC results is slightly higher (~3%) than those of the augmented Burnett solutions. However, the augmented Burnett solutions show much closer agreement with the DSMC results than the Navier–Stokes solutions. In conclusion, the present three-dimensional augmented Burnett solutions agree well with Zhong and Furumoto's axisymmetric augmented Burnett solutions and describe the shock structure closer to the DSMC results than the Navier–Stokes solutions.

Case 4: Effect of Knudsen Number

To further understand the effect of Knudsen number, hypersonic flow past a hemispherical nose with varying Knudsen number is studied. Only the freestream pressure is adjusted to obtain the target Knudsen number, whereas other freestream parameters are kept the same. Computations are performed for Knudsen numbers of 0.0088, 0.0884, and 0.1764. The other flow conditions are the same as for case 1:

$$M_\infty = 10, \quad r_n = 2.53\text{ m}, \quad T_\infty = 230.8\text{ K}, \quad T_w = 1111.0\text{ K}$$

Knudsen numbers and corresponding freestream pressures are

$$Kn_\infty = 0.0088, \qquad P_\infty = 0.2936\text{ N/m}^2$$

$$Kn_\infty = 0.0884, \qquad P_\infty = 0.02925\text{ N/m}^2$$

$$Kn_\infty = 0.1768, \qquad P_\infty = 0.01425\text{ N/m}^2$$

Sutherland's law is applied for viscosity calculations, and all other constants are same as in case 1.

Figures 11–13 show comparisons of the temperature distributions along the stagnation streamline between the Navier–Stokes and the augmented Burnett solutions with varying Knudsen numbers. At $Kn_\infty = 0.0088$, because the flow is almost in the continuum regime, the Navier–Stokes equations predict the flowfield quite well. The differences between the Navier–Stokes and augmented Burnett solutions are very small (~3%) in the temperature distributions. As the Knudsen number increases, the shock layer becomes thicker, and the maximum temperature becomes lower for both the Navier–Stokes and the augmented Burnett solutions. The difference in the temperature distributions between the Navier–Stokes and the augmented Burnett solutions becomes larger as the Knudsen number increases. Figures 11–13 also show that the temperature jump at the stagnation point increases as the Knudsen number increases.

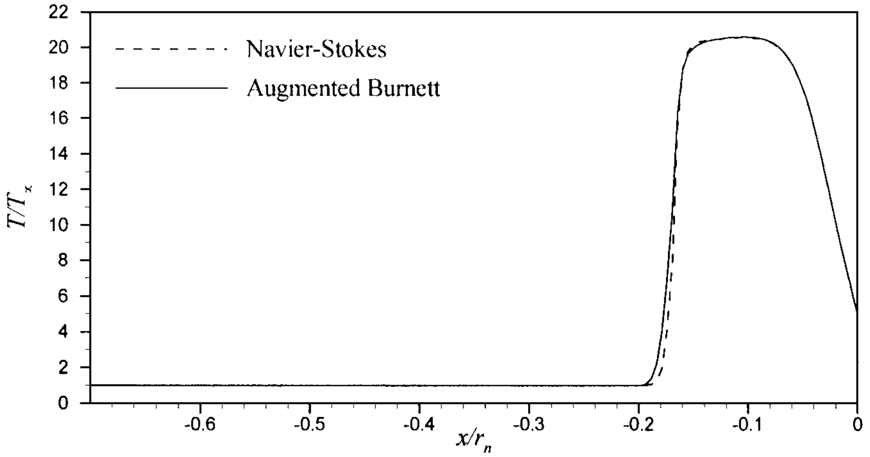

Fig. 11 Comparison of temperature distributions along stagnation streamline for case 4: air, M_∞ = 10, and Kn_∞ = 0.0088.

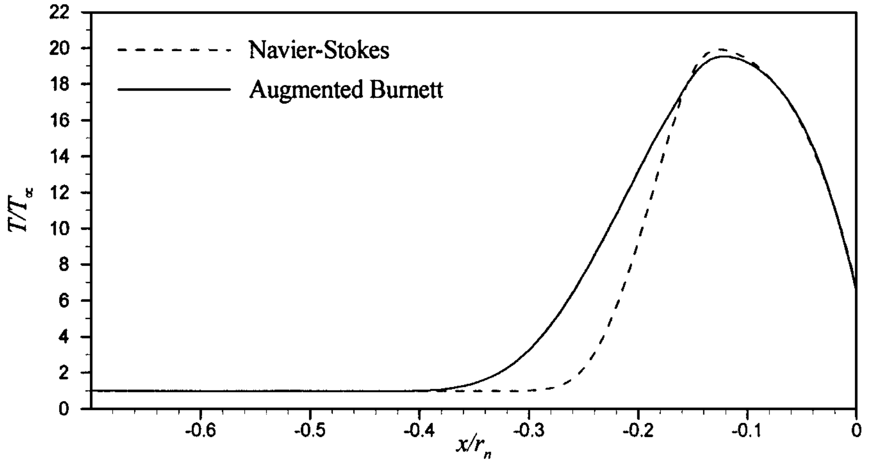

Fig. 12 Comparison of temperature distributions along stagnation streamline for case 4: air, M_∞ = 10, and Kn_∞ = 0.0884.

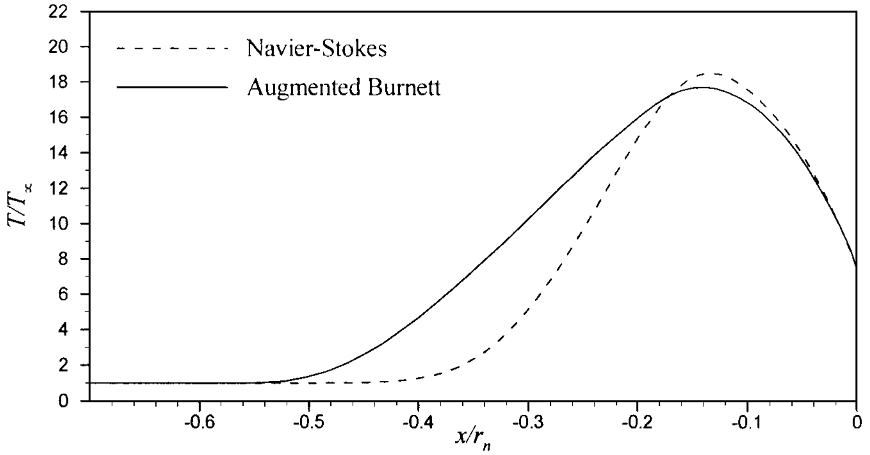

Fig. 13 Comparison of temperature distributions along stagnation streamline for case 4: air, M_∞ = 10 and Kn_∞ = 0.1768.

The temperature jump at the stagnation point is almost negligible at $Kn = 0.0088$. The wall can be considered as a nonslip wall due to the low Knudsen number. Figure 14 shows comparison of temperature contours between the Navier–Stokes and the augmented Burnett solutions at $Kn_\infty = 0.1768$. The augmented Burnett solutions predict about 30% thicker shock layer than the Navier–Stokes solutions at this Knudsen number.

Case 5: Application to a Hemispherical Nose at Angle of Attack

One of the main purpose behind the development of the three-dimensional augmented Burnett code has been to create a capability for accurate prediction of hypersonic flowfields in continuum-transition regime about space orbiters. The axisymmetric augmented Burnett code cannot be used for three-dimensional vehicles at angle of attack. In this case, a true three-dimensional problem of hypersonic flow past a blunt nose at an angle of attack is computed. The hemispherical nose in case 4 is employed again in this calculation. Because the sphere is axisymmetric to any flow direction, the resulting flowfield at an angle of attack is expected to be identical to that of axisymmetric flow. The axisymmetric flow conditions at $Kn_\infty = 0.1768$ from case 4 are selected for this angle-of-attack case. The angle of attack is 15 deg.

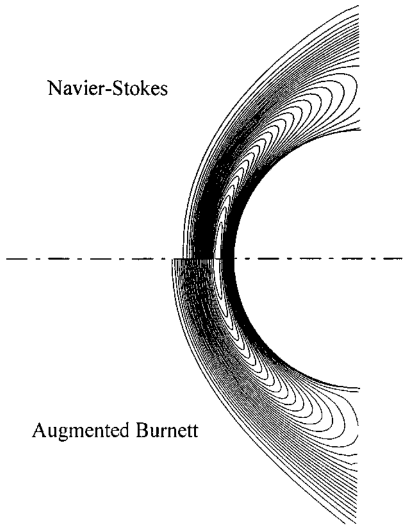

Fig. 14 Comparison of temperature contours for case 4: air, M_∞ = 10, and Kn_∞ = 0.1768 (side view).

Figures 15 and 16 show comparisons of the density and temperature distributions along stagnation streamline between the Navier–Stokes and the augmented Burnett solutions for both 0- and 15-deg angles of attack. The density and temperature distributions from Zhong and Furumoto's[9] axisymmetric augmented Burnett solutions are also compared in Figs. 15 and 16. All of these results agree well with each other for both 0- and 15-deg angles of attack. These calculations show that the present three-dimensional augmented Burnett code predicts the hypersonic flowfields accurately for both the axisymmetric and angle of attack cases.

Case 6: Application to Space Shuttle Reentry Condition

In this case, the augmented Burnett equations are applied to compute the hypersonic flowfield at reentry condition encountered by the nose region of the space shuttle. The computations are compared with the DSMC results of Moss and Bird.[17] The DSMC method accounts for the translational, rotational, vibrational, and chemical nonequilibrium effects.

An equivalent axisymmetric body concept[17] is applied to model the windward centerline of the space shuttle at a given angle of attack. A hyperboloid with nose radius of 1.362 m and asymptotic half-angle of 42.5 deg is employed as the equivalent axisymmetric

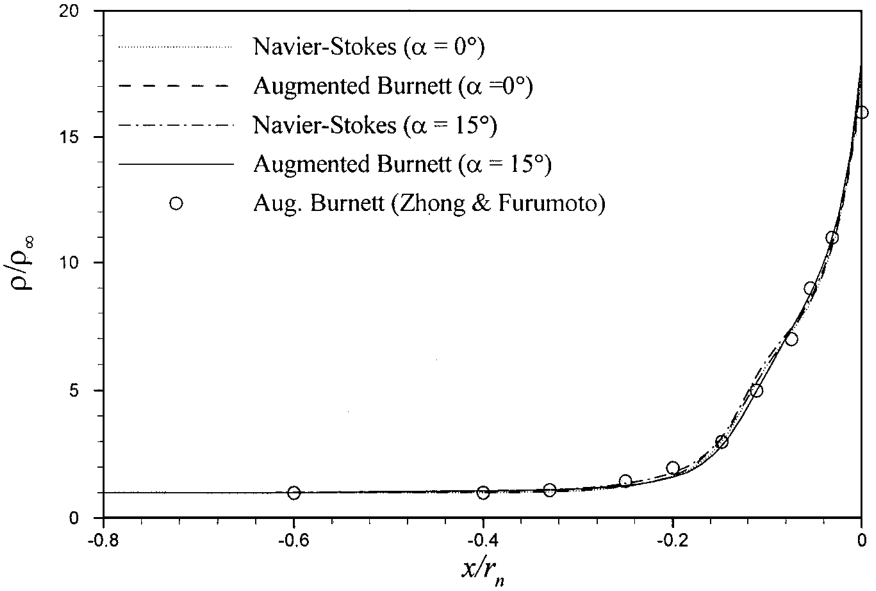

Fig. 15 Density distributions along stagnation streamline for case 5: air, M_∞ = 10, and Kn_∞ = 0.1768.

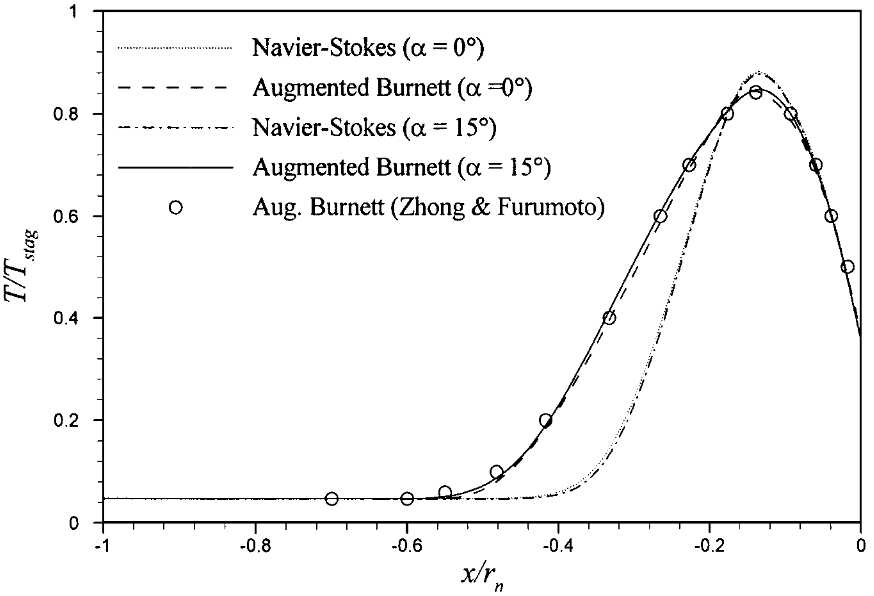

Fig. 16 Temperature distributions along stagnation streamline for case 5: air, M_∞ = 10, and Kn_∞ = 0.1768.

body to simulate the nose of the shuttle. Figure 17 shows the side view of the grid ($61 \times 100 \times 48$ meshes) around the hyperboloid. The freestream conditions at an altitude of 104.93 km as given by Moss and Bird[17] are

$$M_\infty = 25.3, \qquad Kn_\infty = 0.227, \qquad Re_\infty = 163.8$$

$$\rho_\infty = 2.475 \times 10^{-7}\ \mathrm{kg/m^3}, \qquad T_\infty = 223\ \mathrm{K}, \qquad T_w = 560\ \mathrm{K}$$

The viscosity is calculated by the power law given in Eq. (19). The reference viscosity μ_r and the reference temperature T_r are taken as

$$\mu_r = 1.47 \times 10^{-5}\ \mathrm{kg/s \cdot m}, \qquad T_r = 223\ \mathrm{K}$$

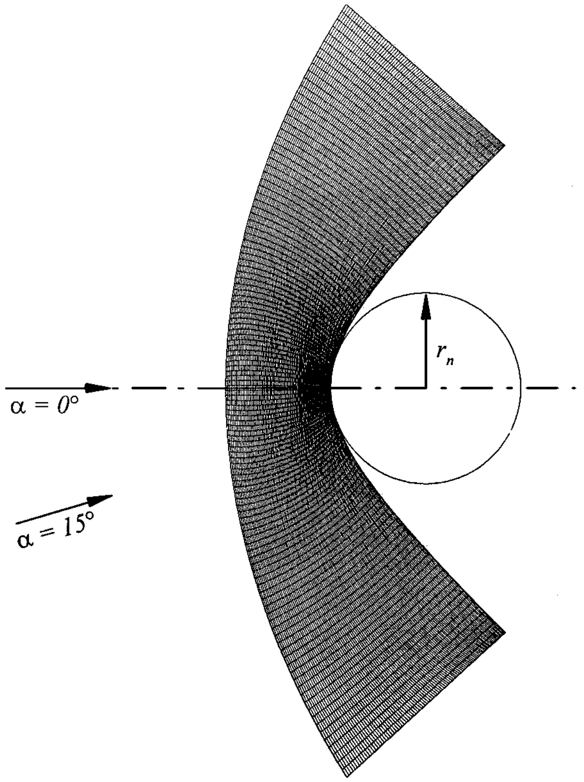

Fig. 17 Side view of the grid ($61 \times 100 \times 48$ mesh) for case 6: air, $M_\infty = 25.3$, $Kn_\infty = 0.227$, and $r_n = 1.362$ m.

Figures 18 and 19 show comparisons of the density and temperature distributions along stagnation streamline between the Navier–Stokes solutions, the augmented Burnett solutions, and the DSMC results. The difference between the augmented Burnett solutions and the DSMC results is significant in both density and temperature distributions. In Fig. 18, density distribution of the DSMC results is lower and smoother than that of the augmented Burnett solutions. In Fig. 19, the DSMC method predicts about 30% thicker shock layer and 9% lower maximum temperature than the augmented Burnett equations. The DSMC results can be considered to be more accurate than the augmented Burnett solutions because the DSMC method accounts for all of the effects of translational, rotational, vibrational, and chemical nonequilibrium whereas the augmented Burnett equations do not. However, the augmented Burnett solutions agree much better with the DSMC results than the Navier–Stokes computations. The difference between the Navier–Stokes and the augmented Burnett solutions in temperature distributions is very significant. The shock layer of the augmented Burnett solutions is almost two times thicker than the Navier–Stokes solutions. The augmented Burnett solutions predict about 11% less maximum temperature than the Navier–Stokes solutions.

The comparisons of temperature jump along the wall are shown in Fig. 20. The difference in the temperature jump distributions between the Navier–Stokes and the augmented Burnett solutions is less than 6%. However, the present calculations using the first-order Maxwell–Smoluchowski slip boundary conditions give about 20% less temperature jump distributions than the DSMC results. These first-order boundary conditions are more appropriate to the Navier–Stokes equations rather than the augmented Burnett equations, which have higher derivatives. The issue of what the appropriate wall boundary conditions are for the augmented Burnett equations remains unsolved at present.

Case 7: Application to the Hyperboloid Nose at Angle of Attack

The hypersonic flow around the hyperboloid nose of the preceding case is computed at an angle of attack. The flow conditions are the same as for case 6 except for the flow direction. The angle of attack for this case is 15 deg.

Unfortunately, neither the computational nor the experimental results are available for this case for the purpose of comparison. Thus, the augmented Burnett calculations at an angle of attack are compared only with the results of the axisymmetric flow case (case 6). Figures 21 and 22 show the comparisons of the density and temperature distributions along the stagnation streamline between the Navier–Stokes and the augmented Burnett solutions for both 0- and 15-deg angles of attack. The shock standoff distance at 15-deg angle

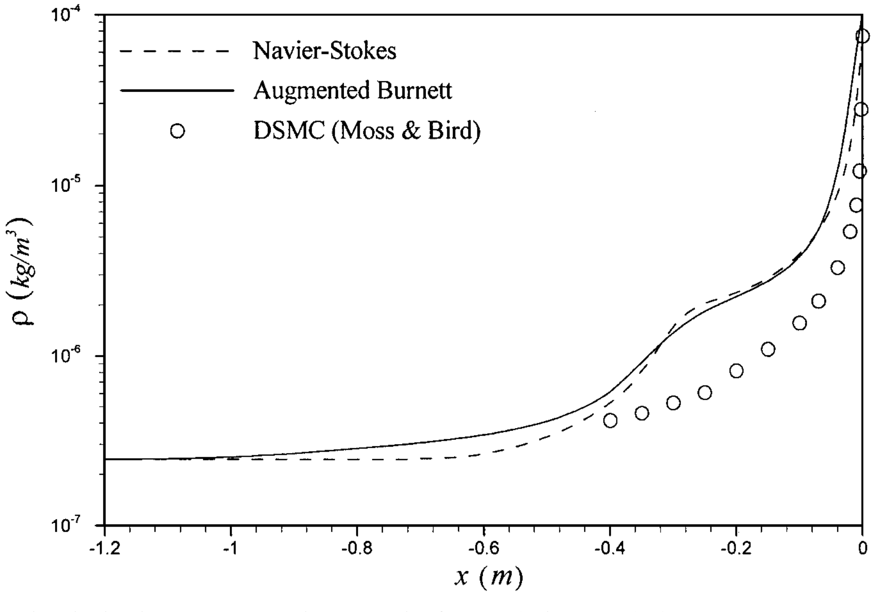

Fig. 18 Density distributions along stagnation streamline for case 6: air, $M_\infty = 25.3$, and $Kn_\infty = 0.227$, and $\alpha = 0$ deg.

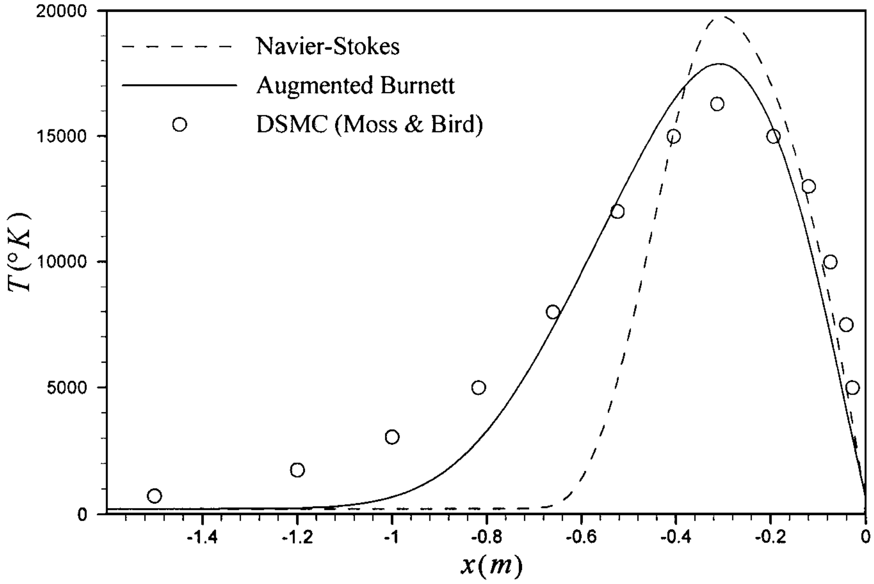

Fig. 19 **Temperature distributions along stagnation streamline for case 6: air, $M_\infty = 25.3$, $Kn_\infty = 0.227$, and $\alpha = 0$ deg.**

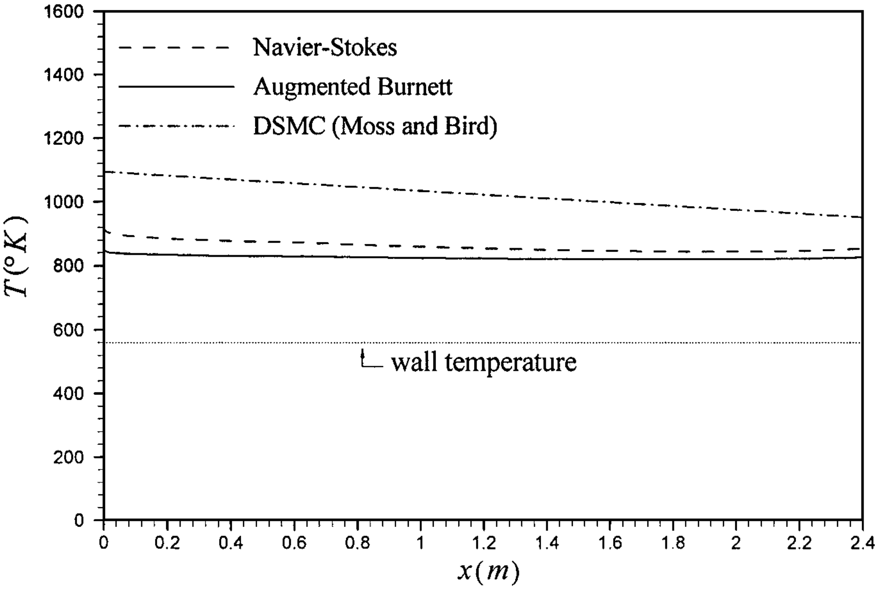

Fig. 20 **Temperature jump along the wall surface for case 6: air, $M_\infty = 25.3$, $Kn_\infty = 0.227$, and $\alpha = 0$ deg.**

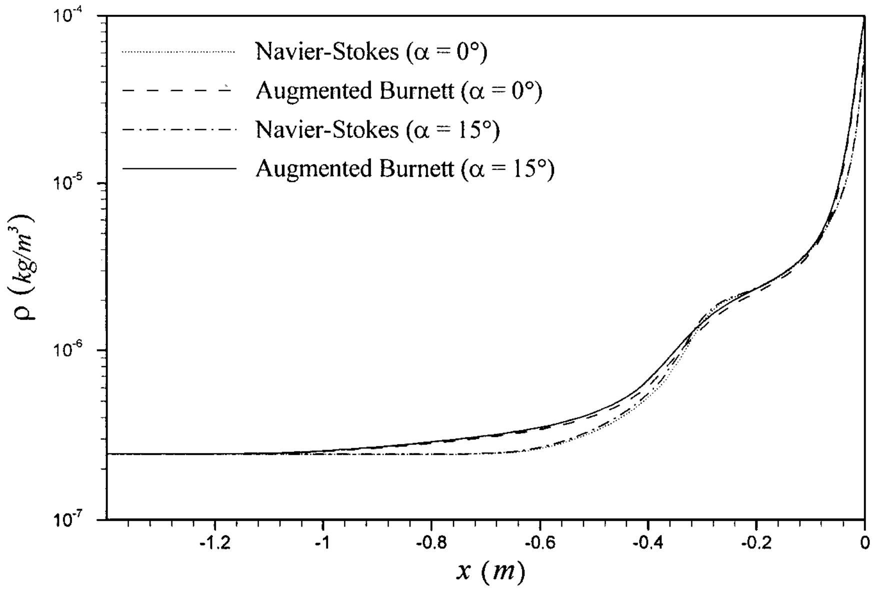

Fig. 21 **Density distributions along stagnation streamline for case 7: air, $M_\infty = 25.3$, and $Kn_\infty = 0.227$.**

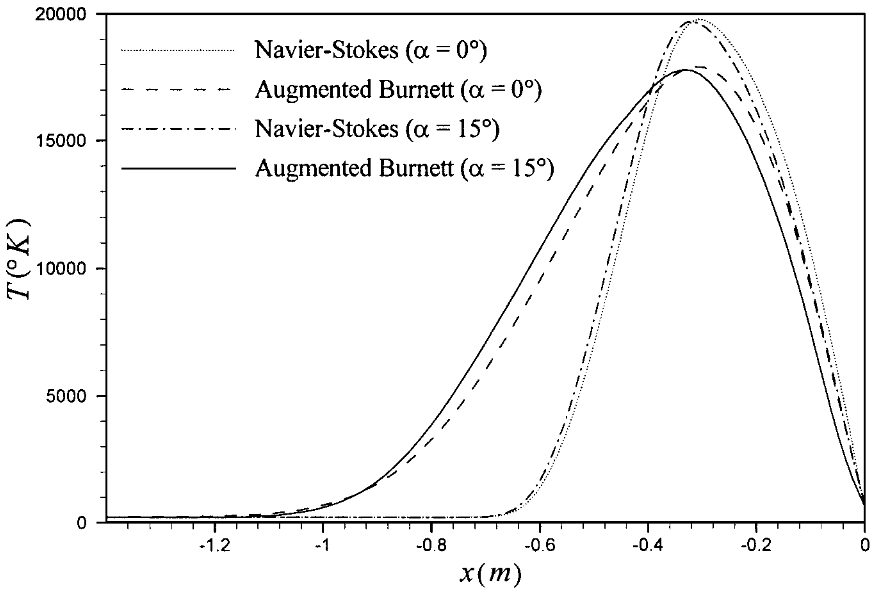

Fig. 22 Temperature distributions along stagnation streamline for case 7: air, M_∞ = 25.3 and Kn_∞ = 0.227.

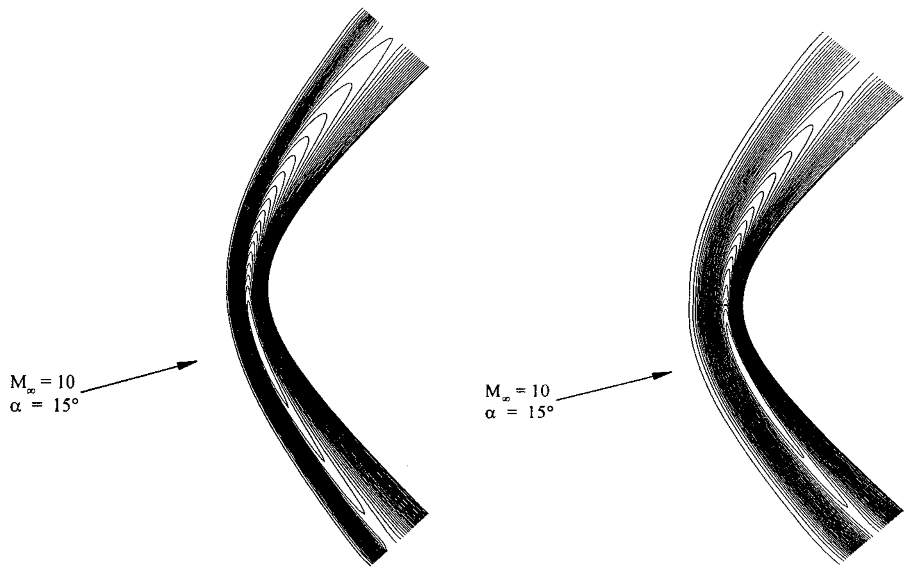

a) Navier–Stokes solution

b) Augmented Burnett solution

Fig. 23 Comparison of temperature contours for case 7: air, M_∞ = 25.3, Kn_∞ = 0.227, and α = 15 deg (side view).

of attack is slightly larger at zero angle of attack because the effective nose radius with regard to the stagnation point is increased.

Figures 23a and 23b show the side view of the temperature contours for the Navier–Stokes and the augmented Burnett solutions at 15-deg angle of attack. The augmented Burnett solutions predict thicker shock than the Navier–Stokes solutions, again as expected.

Conclusions

The three-dimensional augmented Burnett equations have been derived as a set of extended hydrodynamic equations that improve accuracy over the Navier–Stokes equations and the computational efficiency over the DSMC computations for flows in continuum-transition regime. Linearized stability analysis has been carried out to show that the three-dimensional augmented Burnett equations are stable to small perturbations. An explicit time-stepping scheme with the Steger–Warming flux-vector splitting has been employed to discretize the convective terms in the equations; second-order central differencing is used to discretize the viscous stress and heat flux terms. At the wall, the first-order Maxwell–Smoluchowski slip boundary conditions are employed. The code has been applied to compute the three-dimensional hypersonic blunt-body flows at various Knudsen numbers and Mach numbers. The augmented Burnett solutions are compared with the Navier–Stokes solutions and the DSMC results. The following conclusions are made.

1) At a low Knudsen number ($Kn < 0.01$), the difference between the Navier–Stokes solutions and the augmented Burnett solutions is very small. The difference becomes significant as Knudsen number increases ($Kn > 0.1$). The augmented Burnett equations predict thicker shock layer (more than 50%) than the Navier–Stokes equations, especially in temperature distribution; the difference in density distributions between the two solutions is small.

2) The DSMC method predicts about 30% thicker shock layer than the augmented Burnett equations for the temperature distribution. However, the augmented Burnett solutions are significantly closer to the DSMC results than the Navier–Stokes computations in the continuum-transition regime.

3) The temperature jump on the wall surface predicted by the augmented Burnett equations using the first-order Maxwell–Smoluchowski slip boundary conditions is about 20% lower than that obtained with the DSMC simulations. The appropriate wall boundary conditions for higher-order derivatives in the augmented Burnett equations need to be investigated.

These conclusions suggest that the augmented Burnett equations can be applied for hypersonic flows past three-dimensional blunt bodies to improve the accuracy of the computations in the continuum-transition regime, where the Navier–Stokes equations are inaccurate.

Appendix: Coefficients of the Burnett-Order Stress and Heat Flux Terms

The coefficients of the Burnett-order (second-order) stress and heat flux terms shown in Eqs. (11a–11i) are

$$\alpha_1 = \tfrac{2}{3}\omega_1 - \tfrac{14}{9}\omega_2 + \tfrac{2}{9}\omega_6, \qquad \alpha_2 = \tfrac{1}{3}\omega_2 + \tfrac{1}{12}\omega_6$$

$$\alpha_3 = \tfrac{1}{3}\omega_2 + \tfrac{1}{12}\omega_6, \qquad \alpha_4 = -\tfrac{2}{3}\omega_2 + \tfrac{1}{12}\omega_6$$

$$\alpha_5 = -\tfrac{1}{3}\omega_1 + \tfrac{7}{9}\omega_2 - \tfrac{1}{9}\omega_6, \qquad \alpha_6 = \tfrac{1}{3}\omega_2 - \tfrac{1}{6}\omega_6$$

$$\alpha_7 = -\tfrac{2}{3}\omega_2 + \tfrac{1}{12}\omega_6, \qquad \alpha_8 = \tfrac{1}{3}\omega_2 - \tfrac{1}{6}\omega_6$$

$$\alpha_9 = -\tfrac{1}{3}\omega_1 + \tfrac{7}{9}\omega_2 - \tfrac{1}{9}\omega_6, \qquad \alpha_{10} = \tfrac{1}{3}\omega_1 + \tfrac{2}{9}\omega_2 - \tfrac{2}{9}\omega_6$$

$$\alpha_{11} = -\tfrac{2}{3}\omega_1 - \tfrac{4}{9}\omega_2 + \tfrac{4}{9}\omega_6, \qquad \alpha_{12} = \tfrac{1}{3}\omega_1 + \tfrac{2}{9}\omega_2 - \tfrac{2}{9}\omega_6$$

$$\alpha_{13} = -\tfrac{2}{3}\omega_2 + \tfrac{1}{6}\omega_6, \qquad \alpha_{14} = \tfrac{4}{3}\omega_2 - \tfrac{1}{3}\omega_6$$

$$\alpha_{15} = -\tfrac{2}{3}\omega_2 + \tfrac{1}{6}\omega_6, \qquad \alpha_{16} = -\tfrac{2}{3}\omega_2 + \tfrac{2}{3}\omega_3$$

$$\alpha_{17} = \tfrac{1}{3}\omega_2 - \tfrac{1}{3}\omega_3, \qquad \alpha_{18} = \tfrac{1}{3}\omega_2 - \tfrac{1}{3}\omega_3, \qquad \alpha_{19} = -\tfrac{2}{3}\omega_2$$

$$\alpha_{20} = \tfrac{1}{3}\omega_2, \qquad \alpha_{21} = \tfrac{1}{3}\omega_2, \qquad \alpha_{22} = \tfrac{2}{3}\omega_2, \qquad \alpha_{23} = -\tfrac{1}{3}\omega_2$$

$$\alpha_{24} = -\tfrac{1}{3}\omega_2, \qquad \alpha_{25} = \tfrac{2}{3}\omega_4 + \tfrac{2}{3}\omega_5, \qquad \alpha_{26} = -\tfrac{1}{3}\omega_4 - \tfrac{1}{3}\omega_5$$

$$\alpha_{27} = -\tfrac{1}{3}\omega_4 - \tfrac{1}{3}\omega_5, \qquad \alpha_{28} = -\tfrac{2}{3}\omega_2 + \tfrac{2}{3}\omega_4$$

$$\alpha_{29} = \tfrac{1}{3}\omega_2 - \tfrac{1}{3}\omega_4, \qquad \alpha_{30} = \tfrac{1}{3}\omega_2 - \tfrac{1}{3}\omega_4$$

$$\beta_1 = \tfrac{1}{2}\omega_1 - \tfrac{5}{3}\omega_2 + \tfrac{1}{6}\omega_6, \qquad \beta_2 = \tfrac{1}{2}\omega_1 - \tfrac{5}{3}\omega_2 + \tfrac{1}{6}\omega_6$$

$$\beta_3 = -\omega_2 + \tfrac{1}{4}\omega_6, \qquad \beta_4 = \tfrac{1}{2}\omega_1 - \tfrac{2}{3}\omega_2 + \tfrac{1}{6}\omega_6$$

$$\beta_5 = \tfrac{1}{2}\omega_1 - \tfrac{2}{3}\omega_2 + \tfrac{1}{6}\omega_6, \qquad \beta_6 = \tfrac{1}{4}\omega_6$$

$$\beta_7 = \tfrac{1}{2}\omega_1 + \tfrac{1}{3}\omega_2 - \tfrac{1}{3}\omega_6, \qquad \beta_8 = \tfrac{1}{2}\omega_1 + \tfrac{1}{3}\omega_2 - \tfrac{1}{3}\omega_6$$

$$\beta_9 = -\omega_2 + \tfrac{1}{4}\omega_6, \qquad \beta_{10} = -\omega_2 + \tfrac{1}{4}\omega_6, \qquad \beta_{11} = -\omega_2 + \omega_3$$

$$\beta_{12} = -\omega_2, \qquad \beta_{13} = \omega_4 + \omega_5, \qquad \beta_{14} = \omega_2$$

$$\beta_{15} = -\tfrac{1}{2}\omega_2 + \tfrac{1}{2}\omega_4, \qquad \beta_{16} = -\tfrac{1}{2}\omega_2 + \tfrac{1}{2}\omega_4$$

$$\gamma_1 = \theta_1 + \tfrac{8}{3}\theta_2 + \tfrac{2}{3}\theta_3 + \tfrac{2}{3}\theta_5, \qquad \gamma_2 = \theta_1 + \tfrac{2}{3}\theta_2 - \tfrac{1}{3}\theta_3 - \tfrac{1}{3}\theta_5$$

$$\gamma_3 = \theta_1 + \tfrac{2}{3}\theta_2 - \tfrac{1}{3}\theta_3 - \tfrac{1}{3}\theta_5, \qquad \gamma_4 = 2\theta_2 + \tfrac{1}{2}\theta_3 + \tfrac{1}{2}\theta_5$$

$$\gamma_5 = \tfrac{1}{2}\theta_3 + \tfrac{1}{2}\theta_5, \qquad \gamma_6 = 2\theta_2 + \tfrac{1}{2}\theta_3 + \tfrac{1}{2}\theta_5, \qquad \gamma_7 = \tfrac{1}{2}\theta_3 + \tfrac{1}{2}\theta_5$$

$$\gamma_8 = \tfrac{2}{3}\theta_2 + \tfrac{2}{3}\theta_4, \qquad \gamma_9 = \tfrac{1}{2}\theta_4, \qquad \gamma_{10} = \tfrac{1}{2}\theta_4, \qquad \gamma_{11} = \tfrac{2}{3}\theta_2 + \tfrac{1}{6}\theta_4$$

$$\gamma_{12} = \tfrac{2}{3}\theta_2 + \tfrac{1}{6}\theta_4, \qquad \gamma_{13} = \tfrac{2}{3}\theta_3, \qquad \gamma_{14} = -\tfrac{1}{3}\theta_3, \qquad \gamma_{15} = -\tfrac{1}{3}\theta_3$$

$$\gamma_{16} = \tfrac{1}{2}\theta_3, \qquad \gamma_{17} = \tfrac{1}{2}\theta_3, \qquad \gamma_{18} = \tfrac{1}{2}\theta_3, \qquad \gamma_{19} = \tfrac{1}{2}\theta_3$$

where the coefficients ω_i and θ_i are given in Table A1.

Table A1 Coefficients in the Burnett equations

Coefficient	Maxwellian gas	Hard-sphere gas
ω_1	$\frac{10}{3}$	4.056
ω_2	2	2.028
ω_3	3	2.418
ω_4	0	0.681
ω_5	3	0.219
ω_6	8	7.424
θ_1	$\frac{75}{8}$	11.644
θ_2	$-\frac{45}{8}$	−5.822
θ_3	−3	−3.090
θ_4	3	2.418
θ_5	$\frac{117}{4}$	25.157

References

[1] Chapman, S., and Cowling, T. G., *The Mathematical Theory of Non-Uniform Gases*, Cambridge Univ. Press, New York, 1960.

[2] Kogan, M. N., *Rarefied Gas Dynamics*, Plenum, New York, 1969.

[3] Bird, G. A., "Monte Carlo Simulation of Gas Flows," *Annual Review of Fluid Mechanics*, Vol. 10, 1978, pp. 11–31.

[4] Bird, G. A., *Molecular Gas Dynamics and the Direct Simulation of Gas Flows*, Oxford Science, New York, 1994.

[5] Fiscko, K. A., and Chapman, D. R., "Hypersonic Shock Structure with Burnett Terms in the Viscous Stress and Heat Flux," AIAA Paper 88-2733, June 1988.

[6] Fiscko, K. A., and Chapman, D. R., "Comparison of Burnett, Super-Burnett and Monte Carlo Solutions for Hypersonic Shock Structure," *Rarefied Gas Dynamics: Theoretical and Computational Techniques*, Vol. 118, Progress in Astronautics and Aeronautics, AIAA, Washington, DC, 1989, pp. 374–395.

[7] Bobylev, A. V., "The Chapman–Enskog and Grad Methods for Solving the Boltzmann Equation," *Soviet Physics—Doklady*, Vol. 27, Jan. 1982.

[8] Zhong, X., "Development and Computation of Continuum Higher Order Constitutive Relations for High-Altitude Hypersonic Flow," Ph.D. Dissertation, Dept. of Aeronautics and Astronautics, Stanford Univ., Stanford, CA, Aug. 1991.

[9] Zhong, X., and Furumoto, G., "Solutions of the Burnett Equations for Axisymmetric Hypersonic Flow Past Spherical Blunt Bodies," AIAA Paper 94-1959, June 1994.

[10] Comeaux, K. A., Chapman, D. R., and MacCormack, R. W., "An Analysis of the Burnett Equations Based on the Second Law of Thermodynamics," AIAA Paper 95-0415, Jan. 1995.

[11] Yun, K.-Y., Agarwal, R. K., and Balakrishnan, R., "Augmented Burnett and Bhatnagar–Gross–Krook–Burnett for Hypersonic Flow," *Journal of Thermophysics and Heat Transfer*, Vol. 12, No. 3, 1998, pp. 328–335.

[12] Agarwal, R. K., Yun, K.-Y., and Balakrishnan, R., "Beyond Navier–Stokes: Burnett Equations for Flow Simulations in Continuum-Transition Regime," AIAA Paper 99-3580, June 1999.

[13] Yun, K.-Y., "Numerical Simulation of 3-D Augmented Burnett Equations for Hypersonic Flow in Continuum-Transition Regime," Ph.D. Dissertation, Dept. of Aerospace Engineering, Wichita State Univ., Wichita, KS, Dec. 1999.

[14] Schaaf, S. A., and Chambre, P. L., *Flow of Rarefied Gases*, Princeton Univ. Press, Princeton, NJ, 1966.

[15] Steger, J. L., and Warming, R. F., "Flux Vector Splitting of the Inviscid Gas Dynamics Equations with Application to Finite-Difference Methods," *Journal of Computational Physics*, Vol. 40, No. 2, 1981, pp. 263–293.

[16] Vogenitz, F. W., and Takara, G. Y., "Monte Carlo Study of Blunt Body Hypersonic Viscous Shock Layers," *Rarefied Gas Dynamics*, Vol. 2, Editrice Tecnico Scientifica, Pisa, Italy, 1971, pp. 911–918.

[17] Moss, J. N., and Bird, G. A., "Direct Simulation of Transitional Flow for Hypersonic Reentry Conditions," AIAA Paper 84-0223, Jan. 1984.

J. C. Taylor
Associate Editor